



Cite this: *RSC Adv.*, 2017, 7, 34138

# One-pot synthesis and first-principles elasticity analysis of polymorphic MnO<sub>2</sub> nanorods for tribological assessment as friction modifiers

Niraj Kumar,<sup>a</sup> Shubrajit Bhaumik,<sup>c</sup> Arijit Sen,<sup>\*ab</sup> A. Pooja Shukla<sup>ab</sup> and S. D. Pathak<sup>c</sup>

One-pot synthesis of single-crystalline  $\alpha$  and  $\beta$ -MnO<sub>2</sub> nanorods was carried out by selectively varying the acidic concentrations. Ultrafine one dimensional nanorods with diameters of about 10–40 nm are achieved. The respective phases of the nanorods were then altered through simple optimization in the molar concentration of H<sub>2</sub>SO<sub>4</sub>. Morphological transition from microstructure to nanostructure is also examined by changing the acid concentration from high to low. Elastic and tribological properties of these nanomaterials were subsequently explored, with a view to their possible applications as nanoadditives in green lubricants. While  $\beta$ -MnO<sub>2</sub> nanorods showed a reduction in the coefficient of friction by about 15%,  $\alpha$ -MnO<sub>2</sub> nanorods turned out to be even better nanoadditives yielding a reduction of as high as 30%. Moreover, both the polymorphs of MnO<sub>2</sub> nanostructures led to lower roughness when used as nanoadditives in the base oil. Our analysis suggests that such enhancement of antiwear properties originates primarily from the mutual interplay between the rolling action and the protective layer formation by respective polymorphs of quasi-1D MnO<sub>2</sub>. From the first-principles analysis, we envisage that  $\alpha$ -MnO<sub>2</sub> nanorods may potentially serve as efficient nanoadditives in comparison with  $\beta$ -MnO<sub>2</sub> nanorods due to superior elastic properties of the former.

Received 19th April 2017  
Accepted 30th June 2017

DOI: 10.1039/c7ra04401a

rsc.li/rsc-advances

## 1 Introduction

MnO<sub>2</sub> nanostructures are one of the most stable manganese oxides in nature.<sup>1</sup> The morphology of MnO<sub>2</sub> is often an influential factor due to the presence of highly active sites which offers promising electrokinetics and catalytic activities.<sup>2</sup> In particular, the rich polymorphism and structural flexibility with excellent physical and chemical properties of these compounds<sup>3,4</sup> have opened the door for a wide range of applications in energy storage systems,<sup>5–13</sup> fuel cell catalysis,<sup>14–17</sup> water treatment,<sup>18,19</sup> biosensing<sup>20,21</sup> *etc.* The past few decades have seen numerous techniques for the synthesis and characterization of these nanomaterials including sol–gel templating,<sup>22</sup> thermal decomposition,<sup>23</sup> refluxing,<sup>24</sup> solvent-free solid reaction,<sup>25</sup> electrodeposition<sup>26</sup> and hydrothermal methods.<sup>27–31</sup> Among these, the hydrothermal method can well be a preferred choice because of its effectiveness, simplicity and low cost. Ramachandran *et al.*<sup>32</sup> have used the hydrothermal method to grow  $\alpha$ -phase manganese dioxide nanorods over nitrogen doped graphite nanowires. We have recently developed<sup>33,34</sup> MnO<sub>2</sub>

nanorods and nanowires using a facile hydrothermal treatment without resorting to any seed, capping agent or template.

As mentioned earlier, the properties like rich polymorphism and structural flexibility exhibited by MnO<sub>2</sub> nanostructures can make it to withstand extreme pressure with high level of anti wear properties, which is a prerequisite for a good lubricant. This brings the need to explore the tribological properties of MnO<sub>2</sub> nanostructure as friction modifiers. Although MnO<sub>2</sub> nanorods have long been seen as an important electrode material for energy storage, its role as an efficient additive in lubrication has not been studied much. Lubrication is known to be one of the most important mechanical processes in controlling the wear of various machineries.

Commercially petroleum oils are used extensively as lubricants but have major drawback as they are conventionally non-renewable energy sources. This has prompted researches to explore green or renewable energy alternatives.<sup>35</sup> Owing to this, biodegradable palm or vegetable oil as lubricants have gained much attention due to their better lubricating properties such as high-index viscosity, low volatility and good lubricity and of course for being perfect green or renewable energy alternatives.<sup>36–38</sup> However, their anti-wear properties under extreme pressure as against commercial petroleum oils are not so impressive.<sup>39</sup> Zulkifli *et al.* demonstrated that palm oils suffer from poor anti-wear properties than commercial lubricants.<sup>40</sup> Recent progress in synthesis of nanomaterials provides the researchers a new prospect to overcome the above problem with

<sup>a</sup>SRM Research Institute, SRM University, Kattankulathur-603203, India. E-mail: arjit.s@res.srmuniv.ac.in

<sup>b</sup>Department of Physics and Nanotechnology, SRM University, Kattankulathur-603203, India

<sup>c</sup>Department of Mechanical Engineering, SRM University, Kattankulathur-603203, India



the origin of nanotribology. Additives at nanoscale regime are supposed to improve the anti-wear properties of base oil on mixing due to their high surface activities as compared to their bulk counterpart.<sup>41–44</sup> Gulzar *et al.* have reported an enhancement in the anti-wear property of palm oil by adding CuO and MoS<sub>2</sub> nanoparticles as additives.<sup>35</sup> Various mechanism for nanoparticles based lubricants, which are responsible for protecting the metal to metal surfaces, include ball bearing effect,<sup>45–47</sup> protective film effect,<sup>48–52</sup> mending and polishing effect<sup>53</sup> *etc.* In the works of Zhang *et al.*,<sup>54</sup> the friction and wear properties of the base oil get enhanced with the use of WS<sub>2</sub> nanorods as additives. For Yang *et al.*,<sup>55</sup> high friction and wear properties of base oil are found to occur with the addition of WSe<sub>2</sub> nanorods. They explain the effect of nanorods as additives in terms of the molecule-bearing mechanism of rolling friction and sliding friction of the nanorods between the rubbing surfaces. Besides, Panda *et al.*<sup>56</sup> report the tribological properties of ultra nanocrystalline diamond (UNCD) and diamond nanorod (DNR) films in ambient and nitrogen atmosphere for the implementation of reliable micro- and nano-electromechanical systems (MEMS/NEMS). Also, Liu *et al.*<sup>57</sup> come across the enhanced tribological behaviour of Fe<sub>2</sub>O<sub>3</sub> nanorods based composites with graphene nanosheets and bismaleimides. We have of late reported<sup>58</sup> the possibility of enhancing the tribological properties of castor oil with proper additives. Several recent studies have as well demonstrated that the tribological properties of lubricants can be augmented with the selective use of additives.<sup>59–63</sup>

Our present work focuses on the use of MnO<sub>2</sub> nanorods as additives in base oil (palm oil) for evaluating its tribological properties. Unlike other reported works,<sup>28–32</sup> we developed a common procedure requiring the common time, temperature and precursors to check rich polymorphism by creating two different polymorphs,  $\alpha$  and  $\beta$  of MnO<sub>2</sub> and structure flexibility by drawing 1D nanostructures from bulk to micro and finally to nanoscale with simple optimizations in acidic concentration at the start of hydrothermal reaction without using any external agent. The as prepared nanorods were characterized using FESEM, EDX, XRD, FTIR and TEM while the tribological properties were tested for the nanorods as additives in the base oil using the four-ball-test-rig method<sup>64,65</sup> followed by the three dimensional profilometers and FESEM. In addition, first principles studies were carried out to analyze the elastic properties of  $\alpha$  and  $\beta$ -MnO<sub>2</sub> nanorods. To the best of our knowledge, this work reports for the first time on the tribological aspects of  $\alpha$  and  $\beta$ -MnO<sub>2</sub> nanorods as potential lubrication additives through a comparative analysis.

## 2 Experimental

### 2.1 Materials

Being of analytical grade with high purity, all the reagents, *viz.* Potassium permanganate (KMnO<sub>4</sub>), sodium nitrite (NaNO<sub>2</sub>) and sulphuric acid (H<sub>2</sub>SO<sub>4</sub>), as purchased from Sigma Aldrich, along with biodegradable palm oil, as collected from a local store, were used without any further treatment. All the solutions were made with de-ionized water.

### 2.2 Synthesis

In a typical synthesis, 2 mM KMnO<sub>4</sub> and 3 mM NaNO<sub>2</sub> were mixed in 34 ml of de-ionized water using magnetic stirring. Then, 0.4 M H<sub>2</sub>SO<sub>4</sub> was prepared in 6 ml of de-ionized water and was mixed with the above solution by its dropwise addition at frequent intervals under effective stirring. The hydrothermal process was carried out at 160 °C for 12 h after keeping the above prepared solution in autoclave of 80% capacity. After 12 h of hydrothermal reaction the autoclave was left to be cooled in normal ambient condition. The supernatant was discarded and solid residue was collected upon thoroughly washing with de-ionized water. At last, the synthesized product was given heat treatment at 350 °C for 4 h and termed as sample S1. Sample S2 was prepared following the same synthesis procedures but only changing the molar concentration of H<sub>2</sub>SO<sub>4</sub> to 0.3 M.

### 2.3 Preparation of lubricants

Palm oil is chosen as the base oil for its excellent biodegradable and oxidative properties and also its ease of availability. For the preparation of  $\alpha$ -MnO<sub>2</sub> added palm oil as lubricant, 1 g of the as-prepared  $\alpha$ -MnO<sub>2</sub> nanorods were mixed with 100 ml of palm oil. The prepared solution was probe sonicated for 60 min to agitate the oil and form a homogenous mixture. The solution was further magnetically stirred thoroughly for nearly 60 min. The concentration of the MnO<sub>2</sub> nanorods was 1% by weight (wt). The same procedures were repeated with the  $\beta$ -MnO<sub>2</sub> nanorods to prepare  $\beta$ -MnO<sub>2</sub> nanorods added palm oil as lubricant.

### 2.4 Characterization

X-ray diffraction (XRD) patterns were extracted from PAN analytical X' Pert Pro diffractometer at 30 mA, 40 kV and 1.54 Å Cu-K $\alpha$  rays of wavelength. Morphological studies were carried out *via* 'Quanta 200 FEG FE-SEM' and 'HR-TEM, JEM-2010'. Elemental and functional group analysis was done through 'Bruker 129 eV' with 'Espirit software' and Perkin Elmer Spectrophotometer respectively. The surfaces of the wear scars on the balls after tribo tests were characterized by the FESEM, a non-contact type of profilometer and an optical microscope.

### 2.5 Tribological setup

A four ball test rig was used to determine the anti-wear property of the nanorods based palm oil. The test balls, as used during the experiment, were of AISI 52100 steel with 12.7 mm diameter and approximately 58–60 Rc. Three balls were placed stationary in the lubricant chamber while the fourth ball was fixed in the rotating ball chuck. About 1 g of MnO<sub>2</sub> nanorods (each of  $\alpha$  and  $\beta$  type) were added to 100 ml of palm oil. The suspensions were sonicated using a probe sonicator for 60 minutes followed by stirring using a magnetic stirrer for about 45 minutes. The nanorods suspended oil samples were then poured in the lubricant chamber. Approximately, 30 ml of oil samples were used during each experiment. Enough care was taken to ensure full submersion of all the contact points of the balls. The tests were conducted at 392 N (40 kgf), 1200 rpm and 75 °C for 3600



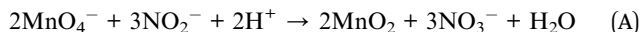
seconds (ASTM D 4172). The data were recorded continuously using a data acquisition system.

## 2.6 Computational details

All the structural relaxations pertaining to  $\alpha$ -MnO<sub>2</sub> and  $\beta$ -MnO<sub>2</sub> quasi-1D nanostructures were performed using the density functional theory (DFT) until the residual forces became smaller than 0.005 eV Å<sup>-1</sup>. The Hamiltonian in the present work was expanded in real space by way of double- $\zeta$  with polarization (DZP) localized pseudoatomic orbitals.<sup>66,67</sup> The exchange–correlation energy was described by the spin-polarized generalized gradient approximation (SGGA). We set the grid mesh cut-off to 300 hartree, the force tolerance to 0.01 eV Å<sup>-1</sup>, and the  $k$ -point sampling to 1 × 1 × 300. For the calculation of the elastic constants, the Lagrangian strain and stress tensor were employed so that the stress could be evaluated numerically as a function of small deformations in the simulation cell. The universal linearly independent coupling strain (ULICS) vectors,<sup>68</sup> as adopted here, ensured that all the stress components and elastic constants were coupled.

## 3 Results and discussions

MnO<sub>2</sub> nanorods were prepared from the redox reaction between permanganate and nitrite ions in the presence of sulphuric acid. In brief, the reaction mechanism can be described as:<sup>21</sup>



According to the Le Chatelier's principle, the feasibility of the reaction depends on the involvement of protons. The protons needed for the reaction is supplied by the sulphuric acid. Here, permanganate ion acts as oxidants and resource of manganese (Mn) element, whereas nitrite ions are used as reducing agents. It is conspicuous that the stoichiometric molar ratio of permanganate to nitrite ions is 2 : 3. Modifications in the amount of proton can lead to the variations in shape, size and phase of the final product.

## 3.1 Structural analysis

The XRD patterns of the samples S1 and S2 prepared with 0.4 and 0.3 M H<sub>2</sub>SO<sub>4</sub> are shown in Fig. 1(a). The diffraction peaks are primarily observed at  $2\theta = 28.68, 37.33$  and  $56.65$  for sample S1 and at  $2\theta = 12.7, 18.1, 28.8, 37.4, 49.8, 60.2$  for sample S2. These prime diffraction peaks can be ascribed to the pure tetragonal phases of  $\beta$ -MnO<sub>2</sub> (JCPDS 24-0735) and  $\alpha$ -MnO<sub>2</sub> (JCPDS 44-0141) for the respective samples S1 and S2. No other peaks of impurities were observed for both the samples, which suggest for their high purity. It is evident that the phase of the synthesized material differs when the same synthesis procedure is followed with different acid concentration. Sample S1, prepared with 0.4 M H<sub>2</sub>SO<sub>4</sub>, has  $\beta$  phase while sample S2, prepared with 0.3 M H<sub>2</sub>SO<sub>4</sub>, has  $\alpha$  phase of MnO<sub>2</sub>. The XRD pattern indicates that the subsequent formation of  $\beta$ -MnO<sub>2</sub> crystals preferably grow along the (110) plane direction though the growth for  $\alpha$ -MnO<sub>2</sub> remains along (211) plane direction.

Interestingly, there was a phase transition to  $\alpha$  phase when the concentration of H<sub>2</sub>SO<sub>4</sub> was reduced to 0.3 M, following the same synthesis procedures. It is apparent that MnO<sub>4</sub><sup>2-</sup> and NO<sub>2</sub><sup>2-</sup> coexisting with the corresponding H<sup>+</sup> ions (eqn (A)) play a crucial role in our synthesis process to determine the crystal structure and morphology of the products. Few assumptions which can be made for the change of phase are detailed below. A certain amount of Mn<sup>4+</sup> ions is required as stabilizing ions for the formation of tunnel structures. In our experiment, the decrease in H<sup>+</sup> ions results in a decrease in the formation rate of Mn<sup>4+</sup> or the growth unit [MnO<sub>6</sub>],<sup>69</sup> which further accounts for a decrease in the formation rate of various crystal faces. This could be the viable reason for the formation of  $\alpha$  phase of MnO<sub>2</sub>, as it has lower crystal faces due to the presence of larger [2 × 2] tunnel structures as against smaller [1 × 1] tunnel structures present in its  $\beta$  phase counterpart.<sup>69</sup> However, a clear insight needs to be done in near future.

## 3.2 Functional group analysis

Infrared spectra of samples S1 and S2 are shown in Fig. 1(b). A common form in transmittance spectra is observed for both the

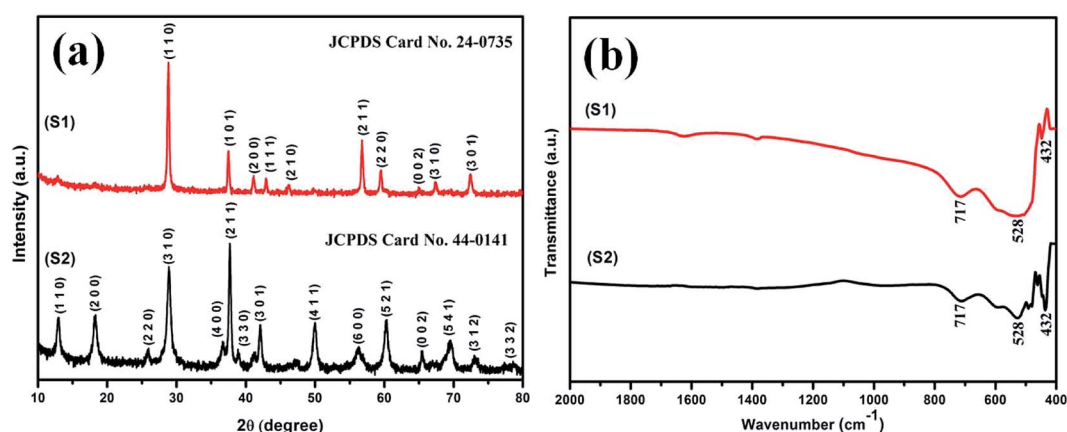


Fig. 1 (a) XRD patterns and (b) FTIR spectroscopy of the samples S1 and S2 prepared using KMnO<sub>4</sub> and NaNO<sub>2</sub> in the molar ratio of 2 : 3 at a temperature of 160 °C for 12 h with H<sub>2</sub>SO<sub>4</sub> in the molar concentration of 0.4 M and 0.3 M, respectively.



samples. The common bands at around 715, 531 and 448  $\text{cm}^{-1}$  can be referred to the metal–oxygen, Mn–O bonding vibrations.<sup>70</sup> No other vibrating bands are present in samples, which reveals for their high purity and is consistent with the XRD analysis.

### 3.3 Morphological analysis

The TEM and HRTEM images shown in Fig. 2(a)–(f) for  $\alpha$  and  $\beta$ - $\text{MnO}_2$  samples confirm their morphologies to be in one dimensional nanorods like shape with diameter in the range of 10–40 nm. The HRTEM image of  $\alpha$ - $\text{MnO}_2$  (see Fig. 2(c)) in growth direction of (310) suggests the  $d$ -spacing of 0.314 nm while that of  $\beta$ - $\text{MnO}_2$  (see Fig. 3(f)) in growth direction of (101) indicates the  $d$ -spacing of 0.24 nm. Both the results match well with their respective JCPDS data.

Energy dispersive X-ray analysis (EDX) of  $\alpha$  and  $\beta$ - $\text{MnO}_2$  nanorods are presented in inset of Fig. 2(c) and (f), respectively. The presence of high intensity peaks for manganese and oxygen elements and the absence of any impurity peaks, indicates that the as-obtained  $\alpha$  and  $\beta$ - $\text{MnO}_2$  nanorods were in pure form with negligible impurities. The results are found in corollary with the XRD data.

For morphological analysis at different acid strengths, different samples were prepared. Fig. 1(a)–(f) shows the FESEM images of samples prepared under different molarities of 1.3, 1.2, 0.9, 0.6, 0.4 and 0.3 M  $\text{H}_2\text{SO}_4$  respectively. FESEM image of the sample prepared with 1.3 M  $\text{H}_2\text{SO}_4$  (Fig. 1(a)) clearly depicts the bulk morphology and rules out presence of any nanostructure. Microstructure in the form of microflakes with microsheets like morphology having thickness of 0.5–1  $\mu\text{m}$  is conspicuous. As seen from Fig. 1(b), microrods like morphology are obtained instead of microsheets when  $\text{H}_2\text{SO}_4$  content is decreased to 1.2 M. These microrods still resemble the bulk

form due to high level of agglomerations and attachments. Microrods having diameters of about 0.3–1  $\mu\text{m}$  with lesser agglomeration and increased finesse can be visualized for the sample prepared at further decreased acidic strength of 0.9 M. The agglomerations are found to be drastically reduced upon decreasing the amount of  $\text{H}_2\text{SO}_4$  to 0.6 M (Fig. 1(c)) and ultra-fine nanorods with diameter in the range of 50–150 nm are obtained. This predicts the possibility of achieving morphologies at nanoscale level by decrease in amount of acid concentration during the synthesis process. The formation of smaller dimensional  $\text{MnO}_2$  structures with slimmer forms was possible due to the restriction imposed on the redox reaction by the decrease in amount of protons ( $\text{H}_2\text{SO}_4$ ) which eventually increases the reduction potential of permanganate ions based on the Nernst equation.<sup>71</sup> Fortunately, the further decrease in  $\text{H}_2\text{SO}_4$  content to 0.4 and 0.3 M leads to reduction in diameters of nanorods (Fig. 1(e) and (f)) and 1D nanorods with diameters in the range of 10–40 nm are formed. Hence, it can be predicted that as the surface energy of nanorods is very high compared to their bulk counterpart, they cannot withstand to form a stable structure under high acidic pressure. Only under optimized conditions with relatively less acidic effect, the probabilities of getting nanostructures are high. In conjugation with the XRD analysis, it is notable that at 0.4 M  $\text{H}_2\text{SO}_4$ ,  $\beta$ - $\text{MnO}_2$  nanorods exist and at 0.3 M  $\text{H}_2\text{SO}_4$ ,  $\alpha$ - $\text{MnO}_2$  nanorods exist.

For studying the growth mechanism of nanorods, FESEM images were captured at different time intervals of 2 h, 5 h and 7 h (Fig. 4(a)–(c)), respectively for the sample prepared at 0.4 M  $\text{H}_2\text{SO}_4$  ( $\beta$ - $\text{MnO}_2$ ). It can be assumed that during the initial stage of hydrothermal reaction *i.e.* after 2 hours, the precursors disintegrates under extreme hydrothermal pressure and nucleates to form nanoparticles (Fig. 4(a)). When the reaction proceeds for 5 h, these nanoparticles self assembled to reduce

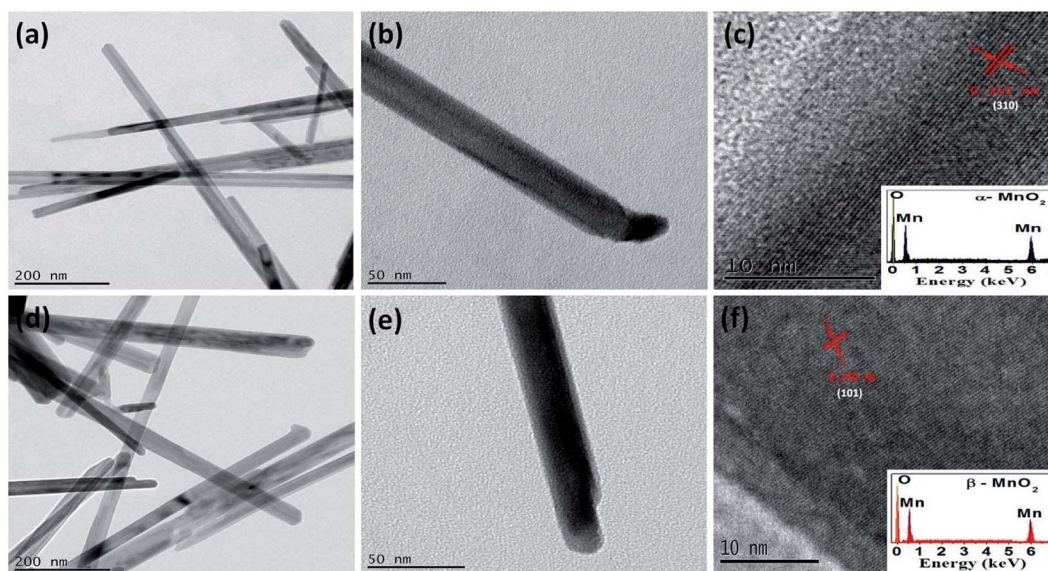


Fig. 2 (a, b) TEM images of  $\alpha$ - $\text{MnO}_2$  at different magnifications, (c) HRTEM image of  $\alpha$ - $\text{MnO}_2$  with growth direction (310),  $d$ -spacing = 0.314 nm and EDX pattern as inset in (c). (d, e) TEM images of  $\beta$ - $\text{MnO}_2$  at different magnifications, (f) HRTEM image of  $\beta$ - $\text{MnO}_2$  with growth direction (101),  $d$ -spacing = 0.24 nm and EDX pattern as inset in (f).



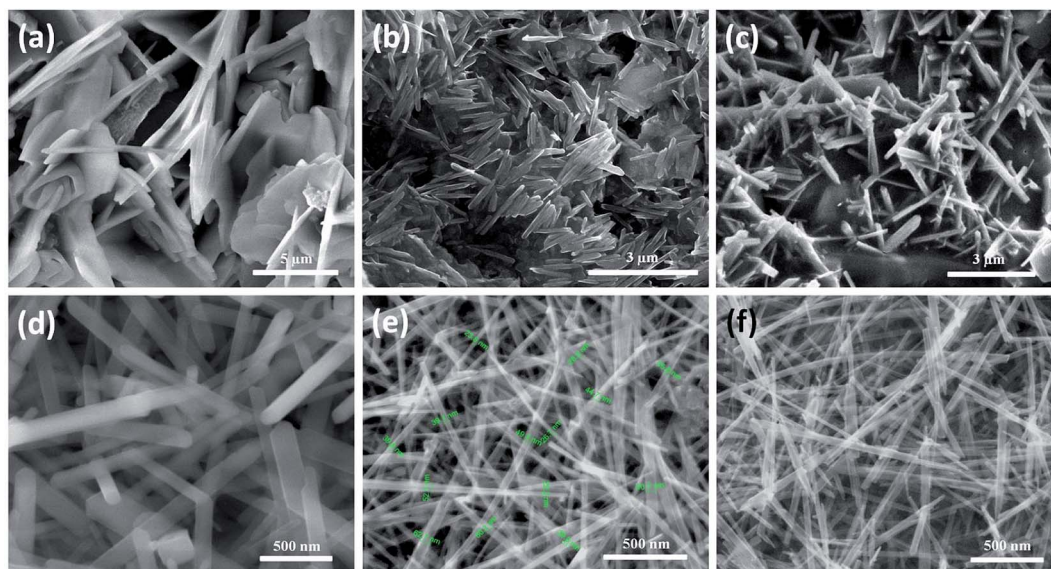


Fig. 3 FESEM images of the final product prepared using  $\text{KMnO}_4$  and  $\text{NaNO}_2$  in the molar ratio of 2 : 3 at a temperature of  $160^\circ\text{C}$  for 12 h with  $\text{H}_2\text{SO}_4$  in the molar concentration of (a) 1.3 M, (b) 1.2 M, (c) 0.9 M, (d) 0.6 M, (e) 0.4 M and (f) 0.3 M.

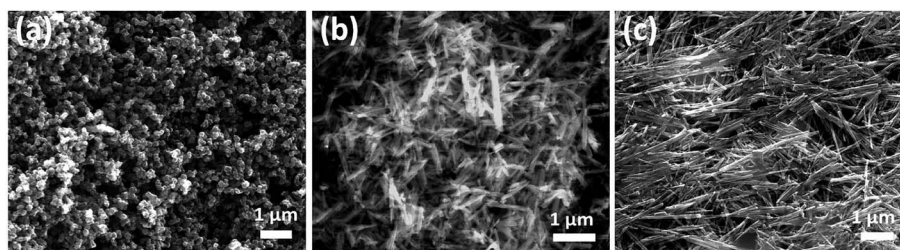


Fig. 4 FESEM images of the sample prepared with 0.4 M  $\text{H}_2\text{SO}_4$  at hydrothermal reaction time of (a) 2 h, (b) 5 h and (c) 7 h.

the interfacial energies generated by their high surface areas and eventually coagulates to form dense mess of aggregated nanorods (Fig. 4(b)). When the reaction further proceeds for 7 h, the aggregated nanorods starts getting their individuality and are fine tuned (Fig. 4(c)). Finally at 12 h of reaction ultrafine nanorods having 10–40 nm diameter can be seen in Fig. 3(e). This can be accounted for the Kirkendall effect. The results are in line with our previous reports.<sup>72</sup>

### 3.4 DFT analysis

As Fig. 5 suggests, quasi-1D nanostructures of  $\alpha$ - and  $\beta$ - $\text{MnO}_2$  are structurally different, which is in good agreement with the HRTEM data (see Fig. 2(c) and (f)). Besides, the chemical potential of  $\alpha$ - $\text{MnO}_2$  is about 40% more than that of  $\beta$ - $\text{MnO}_2$  (see Table 1). For finding the stability of free-standing structures, we resort to the wire tension ( $f$ ) minima, as suggested by Tosatti *et al.*,<sup>73</sup> such that

$$f = (F - \eta N)/L, \quad (1)$$

where,  $\eta$  represents the chemical potential, and  $F$  the free energy associated with  $N$  number of atoms for the wire length of  $L$ . With about 30% lower tension,  $\beta$ - $\text{MnO}_2$  comes out to be

structurally more stable than  $\alpha$ - $\text{MnO}_2$  in its quasi-1D form (see Table 1). Tompsett *et al.*<sup>74</sup> have recently provided some theoretical insight on the stability and electronic structure of  $\beta$ - $\text{MnO}_2$  surfaces. Subsequently, Yuan *et al.*<sup>75</sup> have demonstrated how the oriented attachment plays an important role in the formation of one dimensional tunnelled  $\alpha$ - $\text{MnO}_2$ .

Additionally, Fig. 5 demonstrates that both the phases can exhibit the half-metallic character as well, often suitable for various device applications. However, the spin polarization is more intense along the central strand of  $\alpha$ - $\text{MnO}_2$  unlike the case with  $\beta$ - $\text{MnO}_2$ , where the spin polarization is spread almost all over. It goes well with the recent observation<sup>76</sup> of surface metallicity in  $\text{MnO}_2$ .

To further shed light on the mechanical properties, Table 1 enlists the calculated elastic constants for the two polymorphs of  $\text{MnO}_2$ , based on which the compressibility ( $\Sigma$ ), shear modulus ( $G$ ), Young's modulus ( $Y$ ), and Poisson's ratio ( $V_{xy}$ ) were evaluated using the Voigt–Reuss–Hill averaging scheme.<sup>77</sup> The compressibility can become just double while the shear modulus can drop close to even half the value for  $\beta$ - $\text{MnO}_2$  in comparison with  $\alpha$ - $\text{MnO}_2$ . Similarly, the calculated Young's modulus for  $\alpha$ - $\text{MnO}_2$  turns out to be as much as three times that of  $\beta$ - $\text{MnO}_2$  in quasi-1D conformation.



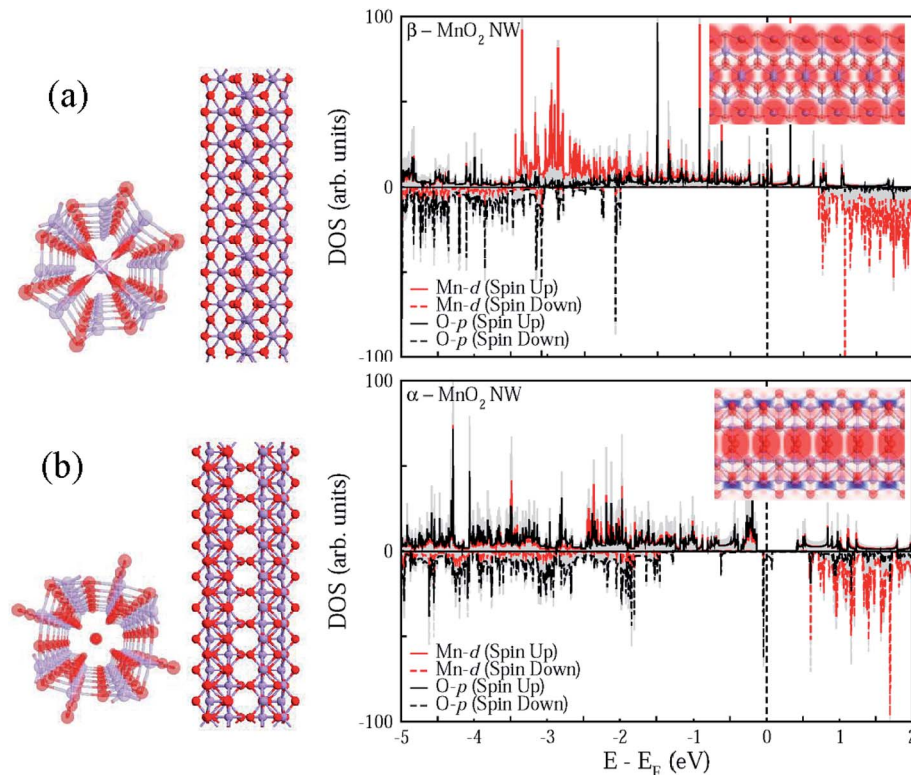


Fig. 5 Calculated quasi-1D nanostructures (top as well as side view) and associated spin-polarized density of states for (a)  $\beta$ -MnO<sub>2</sub> and (b)  $\alpha$ -MnO<sub>2</sub> phases. The electron density difference of each phase for up (red) and down (blue) spins is shown in the respective inset.

**Table 1** Comparative analysis of chemical potential ( $\eta$ ), average magnetic moment ( $m$ ), wire tension ( $f$ ), compressibility ( $\Sigma$ ), shear modulus ( $G$ ), Young's modulus ( $Y$ ) and Poisson's ratio ( $V_{xy}$ ) between quasi-1D nanostructures of  $\alpha$ - and  $\beta$ -MnO<sub>2</sub>, as calculated within the density functional theory

Mechanical properties	$\alpha$ -MnO <sub>2</sub> nanorods	$\beta$ -MnO <sub>2</sub> nanorods
$\eta$ (eV)	5.69	3.98
$m$ ( $\mu_B$ )	1.04	1.95
$f$ (eV $\text{\AA}^{-1}$ )	2.6	1.8
$\Sigma$ (GPa <sup>-1</sup> )	0.14	0.31
$G$ (GPa)	4.5	2.0
$Y$ (GPa)	139.5	38.9
$V_{xy}$	-0.97	-1.38

A detailed study by Riedo *et al.*<sup>78</sup> shows that the change in the friction coefficient of the samples is inversely related to the variations of their Young's modulus. This way, it can be predicted that quasi-1D  $\alpha$ -MnO<sub>2</sub> possesses lower coefficient of friction than  $\beta$ -MnO<sub>2</sub>. It further suggests that  $\alpha$ -MnO<sub>2</sub> should be a promising candidate as lubricant additive in comparison to  $\beta$ -MnO<sub>2</sub>, though the latter has better structural stability in reduced dimensions.

### 3.5 Tribological analysis

The coefficient of friction is calculated according to the following relation:

$$\mu = \left( T\sqrt{6} \right) / 3Wr \quad (2)$$

where,  $\mu$  denotes the coefficient of friction,  $T$  the mean frictional torque (kg mm),  $W$  the applied load (kg) and  $r$  the distance from the centre of the contact ball surface (lower) to the axis of rotation (mm).

**3.5.1 Analysis of frictional properties.** Minimum frictional torque was observed for  $\alpha$ -MnO<sub>2</sub> added palm oil followed by  $\beta$ -MnO<sub>2</sub> added palm oil and pure palm oil (see Fig. 6(a)). The coefficient of friction in case of  $\alpha$ -MnO<sub>2</sub> added palm oil (0.075) was found to be lower than that of  $\beta$ -MnO<sub>2</sub> (0.0881) added palm oil and pure palm oil (0.10419) (see Fig. 6(b)). Error bars shown in Fig. 6(b) account for the average value determined from the three different repeated test values. Lower value of the coefficient of friction, as observed for  $\alpha$ -MnO<sub>2</sub>, is in good agreement with our theoretical analysis. The coefficient of friction in case of  $\alpha$ -MnO<sub>2</sub> and  $\beta$ -MnO<sub>2</sub> nanorods are observed to be 25% and 11.9% lower than the reported coefficient of friction of TiO<sub>2</sub> nanoparticles added palm oil at same additive weight percentage of 0.1%.<sup>79</sup> For a lubricant, lower the coefficient of friction the higher is its lubricity. In this regard we can infer that MnO<sub>2</sub> nanorods can be a better nanoadditive for enhancing the lubricity of biodegradable oils.

The results are also in line with the scar diameters as observed from the Fig. 7(a)–(c), which indicated that surface to surface contact in case of  $\alpha$ -MnO<sub>2</sub> (scar diameter 0.525 mm) is lower than that of  $\beta$ -MnO<sub>2</sub> (scar diameter 0.535 mm) and pure



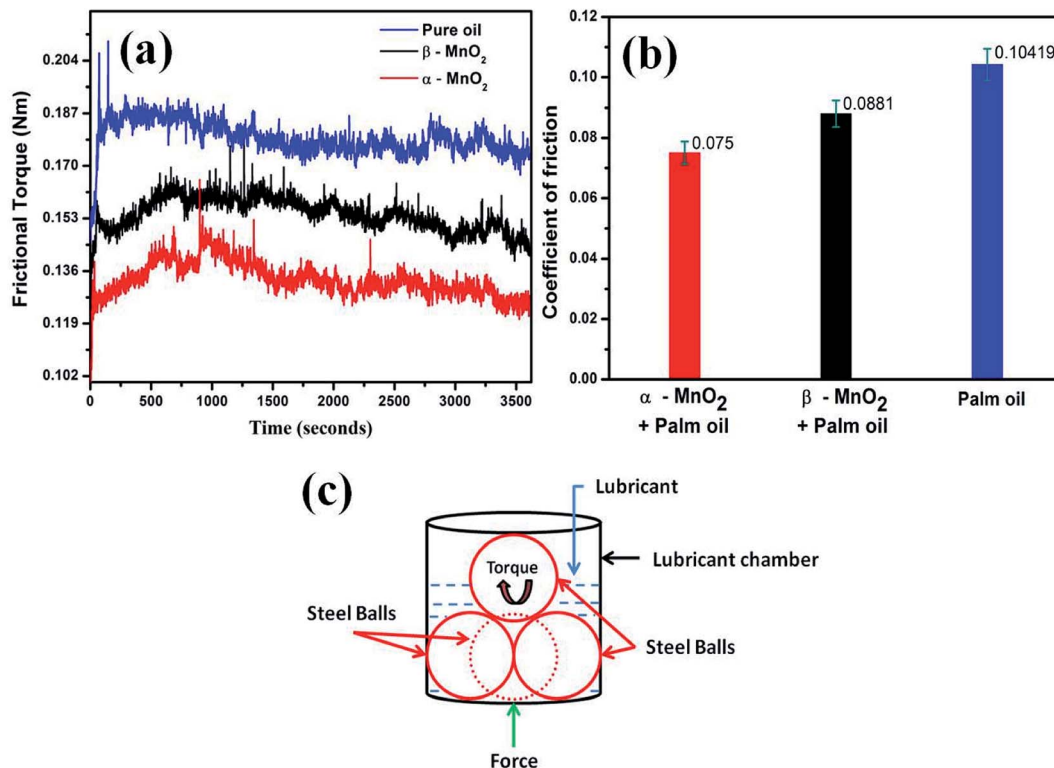


Fig. 6 (a) Frictional torque with respect to time observed using four ball test technique, (b) coefficient of friction of pure palm oil  $\beta$ -MnO<sub>2</sub> added palm oil and  $\alpha$ -MnO<sub>2</sub> added palm oil and (c) schematic outlay of the four-ball test rig.

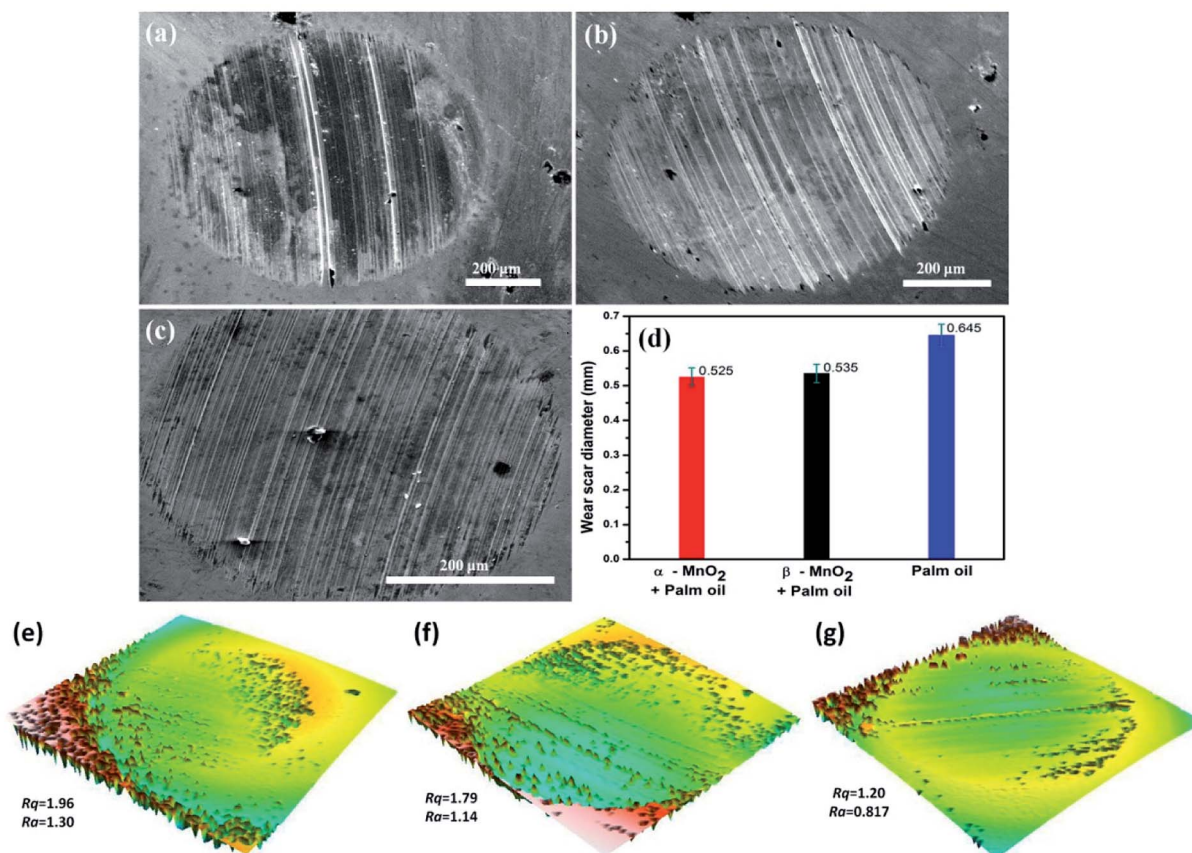


Fig. 7 FESEM images of scar surfaces of the balls tested using (a) pure palm oil, (b)  $\beta$ -MnO<sub>2</sub> added palm oil and (c)  $\alpha$ -MnO<sub>2</sub> added palm oil as lubricants and (d) their respective wear scar diameters. Three dimensional surface morphologies taken using profilometer with line roughness ( $R_q$ ) and average roughness ( $R_a$ ) values for balls tested using (e) pure palm oil, (f)  $\beta$ -MnO<sub>2</sub> added palm oil and (g)  $\alpha$ -MnO<sub>2</sub> added palm oil as lubricants.



palm oil (scar diameter 0.645 mm) (Fig. 7(d)). Error bars account for the average values obtained after three repeated experiments. The scar diameter in case of palm oil is comparable with the reported data (0.62 mm at 40 kgf load).<sup>35</sup> The scar diameters in case of  $\alpha$ -MnO<sub>2</sub> and  $\beta$ -MnO<sub>2</sub> nanorods as additives are found to be 7.9% and 6.14% lower than the reported data,<sup>35</sup> which uses MoS<sub>2</sub> nanoparticles as additives in base palm oil at similar condition. Lower scar diameter directly relates to lowering of wear rate in lubricant. Therefore, the nanorods as additives are expected to show better anti-wear properties.

Further insight into the frictional property through the theoretically calculated Young's modulus can be drawn from Bowden and Tabor theory,<sup>80</sup> as given by

$$f = \tau A, \quad (3)$$

where  $f$  is the force of friction,  $A$  is the area of contact of the contacting bodies and  $\tau$  is the shear strength (critical). From the modified Hertzian theory,<sup>81</sup> the area of contact  $A$  may take the form

$$A = \pi \left[ \frac{3r_c (F_N + F_{adh})}{4E^*} \right]^{2/3}, \quad (4)$$

where  $r_c$ ,  $F_N$ ,  $F_{adh}$  and  $E^*$  are respectively the radius of the contacting body (considered as a sphere which is on a plane), normal load, adhesive load and reduced Young's modulus. For a multi-asperity contact,<sup>82</sup> the frictional force can be written as

$$f = \mu(F_N + F_{adh}) \quad (5)$$

Thus, from eqn (4) and (5), we obtain

$$f = \tau \pi \left( \frac{3r_c}{4E^*} \right) (F_N + F_{adh})^{2/3} \quad (6)$$

From eqn (6), it can be observed that the frictional force is directly proportional to the forces applied and is inversely proportional to the Young's modulus of the contacting bodies. Since,  $\alpha$ -MnO<sub>2</sub> has higher Young's modulus than  $\beta$ -MnO<sub>2</sub>, the frictional force should also be lower in case of  $\alpha$ -MnO<sub>2</sub>, as compared to  $\beta$ -MnO<sub>2</sub>.

**3.5.2 Analysis of surface roughness.** The contact areas of the balls were evaluated for the change in topography after the tribo test using a 3D non-contact type of profilometer. Fig. 7(e)–(g) shows the three dimensional images of the surface topographs of the balls tested using palm oil,  $\beta$ -MnO<sub>2</sub> added palm oil and  $\alpha$ -MnO<sub>2</sub> added palm oil, respectively. The line roughness

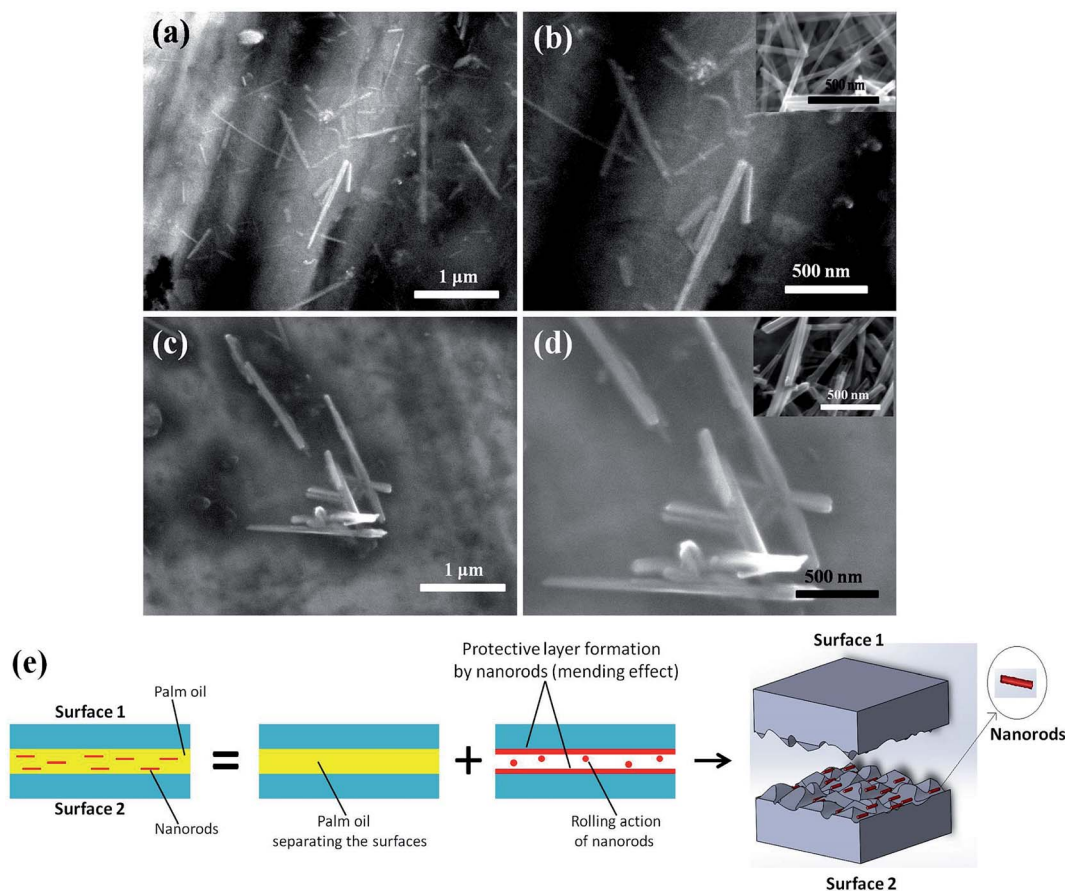


Fig. 8 FESEM images of the deposited nanorods on the scar surfaces of balls tested using (a, b)  $\alpha$ -MnO<sub>2</sub> added palm oil with FESEM image of  $\alpha$ -MnO<sub>2</sub> nanorods as inset in (b), (c, d)  $\beta$ -MnO<sub>2</sub> added palm oil with FESEM image of  $\beta$ -MnO<sub>2</sub> nanorods as inset in (d) and (e) schematic of the mechanisms responsible for enhancement of antiwear property of the base oil by nanorods.



( $R_q$ ) and average roughness ( $R_a$ ) values determined across the sliding direction are represented accordingly. It was observed that the samples which were tested with  $\alpha$ -MnO<sub>2</sub> nanorod based oil had the least roughness ( $R_a$  0.817  $\mu\text{m}$ ,  $R_q$  1.20  $\mu\text{m}$ ) values followed by  $\beta$ -MnO<sub>2</sub> ( $R_a$  1.14  $\mu\text{m}$ ,  $R_q$  1.79  $\mu\text{m}$ ) and pure palm oil ( $R_a$  1.30  $\mu\text{m}$ ,  $R_q$  1.96  $\mu\text{m}$ ). Thus, the nanorods acted as potential friction modifiers at extreme conditions.

$\alpha$ -MnO<sub>2</sub> added palm oil showed better lubricity than  $\beta$ -MnO<sub>2</sub> added palm oil. This is in agreement with the results observed from the scar diameter and coefficient of friction values. Fig. 8(a) and (b) shows the presence of  $\alpha$ -MnO<sub>2</sub> nanorods while Fig. 8(c) and (d) shows the presence of  $\beta$ -MnO<sub>2</sub> nanorods on the scars of tested balls with morphological variations in the nanometer range. Nanorods possessing 1D structure were able to penetrate easily into the intrinsic parts of the contact areas by filling up the small fissures and holes in the rubbing surfaces through the mending effect. A schematic of the mechanism responsible for lowering the coefficient of friction is portrayed in Fig. 8(e). The anchoring behaviour of MnO<sub>2</sub> initiated the formation of *in situ* films which restricted the metal to metal contact, thus, arresting the asperity–asperity contact. As a consequence, nanorods were supposed to form protective layers above the rubbing surfaces which were smoothed enough to exhibit the low coefficient of friction.

In view of nanoscience, a deeper insight can be presumed for the lowering of coefficient of friction with addition of nanorods. It is clear that the additives used were 1D nanostructure and so they must have experienced confinement in density of states by degeneracy of energy levels. This could have increased density of electrons on to the surface, which were confined to move only in one dimension thereby increasing the surface energy. This confined one dimensional movement might have increased the mobility of these high energy electrons which could have developed enough kinetic energy that adds up in the movement of balls and thus helped in decreasing the coefficient of friction.

The FESEM images, as shown in Fig. 8(c) and (d), reveal the noticeable morphological changes in the  $\beta$ -MnO<sub>2</sub> nanorods as compared to  $\alpha$ -MnO<sub>2</sub> nanorods, as shown in Fig. 8(a) and (b). It is evident that the diameter of  $\beta$ -MnO<sub>2</sub> nanorods rose to 80–100 nm range from 10–50 nm range (approximately) after experiencing the anti-wear test. However, in the case of  $\alpha$ -MnO<sub>2</sub> nanorods, there was no noticeable difference in the morphology even after the test. This reveals that  $\alpha$ -MnO<sub>2</sub> nanorods have better elastic properties and superior shock absorbing capabilities in comparison with  $\beta$ -MnO<sub>2</sub> nanorods.

## 4 Conclusions

Ultrafine one dimensional  $\alpha$  and  $\beta$ -MnO<sub>2</sub> nanorods with diameters of about 10–40 nm were successfully obtained by one-pot synthesis. Phase of the MnO<sub>2</sub> nanorods was effectively controlled by altering the molar concentration of H<sub>2</sub>SO<sub>4</sub> at the start of hydrothermal reaction. The work suggests that the nanostructures can exist in relatively low acidic conditions than compared with bulk counterpart. We have explored the tribological aspects of two well-known polymorphic phases of MnO<sub>2</sub> in quasi-1D form. The as prepared nanorods are found to

considerably enhance the lubricity of the base oil. We observe that even a reduction of as high as 30% in the coefficient of friction can happen when  $\alpha$ -MnO<sub>2</sub> nanorods are exploited as nanoadditives in a biodegradable lubricant such as palm oil. The right interplay between the rolling action and the mending effect may be attributed to be the principal mechanism behind such augmentation of the antiwear properties of the base oil, once added with MnO<sub>2</sub> nanorods. Although  $\beta$ -MnO<sub>2</sub> nanorods are structurally more stable than  $\alpha$ -MnO<sub>2</sub> nanorods, the latter come out to be less susceptible to any morphological changes during the antiwear test. Our first principles elasticity analysis reveals that  $\alpha$ -MnO<sub>2</sub> nanorods can be better additives than  $\beta$ -MnO<sub>2</sub> nanorods due primarily to superior elastic properties of the former. This work has established that the polymorphic quasi-1D MnO<sub>2</sub> nanostructures can well be used as effective nanolubricant additives in future.

## Acknowledgements

This work was supported by DST Nano Mission, Govt. of India, via Project No. SR/NM/NS-1062/2012. We are thankful to the National PARAM Supercomputing Facility (NPSF), Centre for Development of Advanced Computing (C-DAC), India, and SRMHPCC for facilitating the high-performance computing.

## References

- 1 T. Zordan and L. G. Hepler, *Chem. Rev.*, 1968, **68**, 737–745.
- 2 G. Gnanakumar, Z. Awan, K. Nahm and J. Xavier, *Biosens. Bioelectron.*, 2014, **53**, 528–534.
- 3 T. Gao, H. Fjellvåg and P. Norby, *Nanotechnology*, 2009, **20**, 055610.
- 4 J. E. Post, *Proc. Natl. Acad. Sci. U. S. A.*, 1999, **96**, 3447–3454.
- 5 S. Chen, J. Zhu and X. Wang, *ACS Nano*, 2010, **4**, 6212–6218.
- 6 L. Feng, Z. Xuan, H. Zhao, Y. Bai, J. Guo, C.-w. Su and X. Chen, *Nanoscale Res. Lett.*, 2014, **9**, 1.
- 7 L.-L. Yu, J.-J. Zhu and J.-T. Zhao, *J. Mater. Chem. A*, 2014, **2**, 9353–9360.
- 8 W. Tang, Y. Hou, X. Wang, Y. Bai, Y. Zhu, H. Sun, Y. Yue, Y. Wu, K. Zhu and R. Holze, *J. Power Sources*, 2012, **197**, 330–333.
- 9 Y. Yang, L. Xiao, Y. Zhao and F. Wang, *Int. J. Electrochem. Sci.*, 2008, **3**, 67–74.
- 10 Y.-C. Chen, Y.-K. Hsu, Y.-G. Lin, Y.-K. Lin, Y.-Y. Horng, L.-C. Chen and K.-H. Chen, *Electrochim. Acta*, 2011, **56**, 7124–7130.
- 11 W. Wei, X. Cui, W. Chen and D. G. Ivey, *Chem. Soc. Rev.*, 2011, **40**, 1697–1721.
- 12 P. Yu, X. Zhang, D. Wang, L. Wang and Y. Ma, *Cryst. Growth Des.*, 2008, **9**, 528–533.
- 13 V. Subramanian, H. Zhu, R. Vajtai, P. Ajayan and B. Wei, *J. Phys. Chem. B*, 2005, **109**, 20207–20214.
- 14 X. Li, B. Hu, S. Suib, Y. Lei and B. Li, *Biochem. Eng. J.*, 2011, **54**, 10–15.
- 15 T. T. Truong, Y. Liu, Y. Ren, L. Trahey and Y. Sun, *ACS Nano*, 2012, **6**, 8067–8077.



- 16 Y. Yuan, H. Li, M. Luo, S. Qin, W. Luo, L. Li and H. Yan, *Water, Air, Soil Pollut.*, 2014, **225**, 1–9.
- 17 Y. Hou, Y. Cheng, T. Hobson and J. Liu, *Nano Lett.*, 2010, **10**, 2727–2733.
- 18 J. B. Fei, Y. Cui, X. H. Yan, W. Qi, Y. Yang, K. W. Wang, Q. He and J. B. Li, *Adv. Mater.*, 2008, **20**, 452–456.
- 19 J. Cao, Q. Mao, L. Shi and Y. Qian, *J. Mater. Chem.*, 2011, **21**, 16210–16215.
- 20 W. Zhang, C. Zeng, M. Kong, Y. Pan and Z. Yang, *Sens. Actuators, B*, 2012, **162**, 292–299.
- 21 J.-J. Feng, P.-P. Zhang, A.-J. Wang, Y. Zhang, W.-J. Dong and J.-R. Chen, *J. Colloid Interface Sci.*, 2011, **359**, 1–8.
- 22 B. B. Lakshmi, C. J. Patrissi and C. R. Martin, *Chem. Mater.*, 1997, **9**, 2544–2550.
- 23 D. Zitoun, N. Pinna, N. Frolet and C. Belin, *J. Am. Chem. Soc.*, 2005, **127**, 15034–15035.
- 24 J. C. Villegas, L. J. Garces, S. Gomez, J. P. Durand and S. L. Suib, *Chem. Mater.*, 2005, **17**, 1910–1918.
- 25 Y.-S. Ding, X.-F. Shen, S. Sithambaram, S. Gomez, R. Kumar, V. M. B. Crisostomo, S. L. Suib and M. Aindow, *Chem. Mater.*, 2005, **17**, 5382–5389.
- 26 M.-S. Wu, J.-T. Lee, Y.-Y. Wang and C.-C. Wan, *J. Phys. Chem. B*, 2004, **108**, 16331–16333.
- 27 B. N. Rao, P. Muralidharan, P. R. Kumar, M. Venkateswarlu and N. Satyanarayana, *Int. J. Electrochem. Sci.*, 2014, **9**, 1207–1220.
- 28 J. G. Zhao, J. Z. Yin and S. G. Yang, *Mater. Res. Bull.*, 2012, **47**, 896–900.
- 29 W. Tang, Y. Hou, X. Wang, Y. Bai, Y. Zhu, H. Sun, Y. Yue, Y. Wu, K. Zhu and R. Holze, *J. Power Sources*, 2012, **197**, 330–333.
- 30 D. Su, H. J. Ahn and G. Wang, *J. Mater. Chem. A*, 2013, **1**, 4845–4850.
- 31 J. Chen, Y. Wang, X. He, S. Xu, M. Fang, X. Zhao and Y. Shang, *Electrochim. Acta*, 2014, **142**, 152–156.
- 32 K. Ramachandran, A. Zahoor, T. Kumar, K. Nahm, A. Balasubramani and G. Kumar, *J. Ind. Eng. Chem.*, 2017, **46**, 19–27.
- 33 N. Kumar, P. Dineshkumar, R. Rameshbabu and A. Sen, *Mater. Lett.*, 2015, **158**, 309–312.
- 34 N. Kumar, P. Dineshkumar, R. Rameshbabu and A. Sen, *RSC Adv.*, 2016, **6**, 7448–7454.
- 35 M. Gulzar, H. Masjuki, M. Varman, M. Kalam, R. Mufti, N. Zulkifli, R. Yunus and R. Zahid, *Tribol. Int.*, 2015, **88**, 271–279.
- 36 P. S. Lathi and B. Mattiasson, *Appl. Catal., B*, 2007, **69**, 207–212.
- 37 M. Fazal, A. Haseeb and H. Masjuki, *Energy Convers. Manage.*, 2013, **67**, 251–256.
- 38 N. Kumar, S. Chauhan, *et al.*, *Proc. Inst. Mech. Eng., Part J*, 2014, **228**, 797–807.
- 39 N. Fox and G. Stachowiak, *Tribol. Int.*, 2007, **40**, 1035–1046.
- 40 N. Zulkifli, M. Kalam, H. Masjuki, M. Shahabuddin and R. Yunus, *Energy*, 2013, **54**, 167–173.
- 41 H. Huang, J. Tu, T. Zou, L. Zhang and D. He, *Tribol. Lett.*, 2005, **20**, 247–250.
- 42 G. Liu, X. Li, B. Qin, D. Xing, Y. Guo and R. Fan, *Tribol. Lett.*, 2004, **17**, 961–966.
- 43 L. Sun, Z. Zhang, Z. Wu and H. Dang, *Mater. Sci. Eng., A*, 2004, **379**, 378–383.
- 44 C. Grossiord, J. Martin, T. Le Mogne and T. Palermo, *Surf. Coat. Technol.*, 1998, **108**, 352–359.
- 45 M. Charoo and M. F. Wani, *Tribol. Ind.*, 2016, **38**, 156–162.
- 46 M. Kandeve, D. Karastoianov, B. Ivanova and V. Pojidaeva, *Proceedings of the 13th International Conference on Tribology–SERBIATRIB'13*, Kragujevac, Serbia, 2013, pp. 31–36.
- 47 L. Rapoport, V. Leshchinsky, M. Lvovsky, O. Nepomnyashchy, Y. Volovik and R. Tenne, *Ind. Lubr. Tribol.*, 2002, **54**, 171–176.
- 48 Y. Wu, W. Tsui and T. Liu, *Wear*, 2007, **262**, 819–825.
- 49 F. Chinas-Castillo and H. Spikes, *J. Tribol.*, 2003, **125**, 552–557.
- 50 Z. S. Hu, R. Lai, F. Lou, L. Wang, Z. Chen, G. Chen and J. Dong, *Wear*, 2002, **252**, 370–374.
- 51 Z. Xiaodong, F. Xun, S. Huaqiang and H. Zhengshui, *Lubr. Sci.*, 2007, **19**, 71–79.
- 52 B. Ginzburg, L. Shibaev, O. Kireenko, A. Shepelevskii, M. Baidakova and A. Sitnikova, *Russ. J. Appl. Chem.*, 2002, **75**, 1330–1335.
- 53 J. Zhou, J. Yang, Z. Zhang, W. Liu and Q. Xue, *Mater. Res. Bull.*, 1999, **34**, 1361–1367.
- 54 L. Zhang, J. Tu, H. Wu and Y. Yang, *Mater. Sci. Eng., A*, 2007, **454**, 487–491.
- 55 J. Yang, H. Yao, Y. Liu and Y. Zhang, *Nanoscale Res. Lett.*, 2008, **3**, 481.
- 56 K. Panda, N. Kumar, K. Sankaran, B. Panigrahi, S. Dash, H.-C. Chen, I.-N. Lin, N.-H. Tai and A. Tyagi, *Surf. Coat. Technol.*, 2012, **207**, 535–545.
- 57 C. Liu, H. Yan, Z. Chen, L. Yuan and T. Liu, *J. Mater. Chem. A*, 2015, **3**, 10559–10565.
- 58 S. Bhaumik, S. Datta and S. D. Pathak, *J. Tribol.*, 2017, **139**(6), 061802.
- 59 J. Hershberger, O. Ajayi and G. Fenske, *Scr. Mater.*, 2005, **53**, 1449–1453.
- 60 L. Joly-Pottuz, F. Dassenoy, M. Belin, B. Vacher, J. Martin and N. Fleischer, *Tribol. Lett.*, 2005, **18**, 477–485.
- 61 F. Dalla Torre, H. Van Swygenhoven, R. Schäublin, P. Spätig and M. Victoria, *Scr. Mater.*, 2005, **53**, 23–27.
- 62 P. Hu, Y. Liu, L. Fu, X. Wang and D. Zhu, *Appl. Phys. A: Mater. Sci. Process.*, 2005, **80**, 35–38.
- 63 Z. Li, X. Tao, Y. Cheng, Z. Wu, Z. Zhang and H. Dang, *Mater. Sci. Eng., A*, 2005, **407**, 7–10.
- 64 F. Ilie and C. Covaliu, *Lubricants*, 2016, **4**, 12.
- 65 A. Dongare and G. Vikhe Patil, *Int. J. Eng. Res. Dev.*, 2012, **6**–11.
- 66 *Atomistix ToolKit version 2015.1*, <http://www.quantumwise.com>.
- 67 M. Brandbyge, J.-L. Mozos, P. Ordejón, J. Taylor and K. Stokbro, *Phys. Rev. B: Condens. Matter Mater. Phys.*, 2002, **65**, 165401.
- 68 R. Yu, J. Zhu and H. Ye, *Comput. Phys. Commun.*, 2010, **181**, 671–675.



- 69 X. Wang and Y. Li, *J. Am. Chem. Soc.*, 2002, **124**(12), 2880–2881.
- 70 Y.-J. Huang and W.-S. Li, *J. Inorg. Mater.*, 2013, **28**, 341–346.
- 71 C. M. McShane and K.-S. Choi, *J. Am. Chem. Soc.*, 2009, **131**, 2561–2569.
- 72 N. Kumar, A. Sen, K. Rajendran, R. Rameshbabu, J. Ragupathi, H. Therese and T. Maiyalagana, *RSC Adv.*, 2017, **7**, 25041.
- 73 E. Tosatti, S. Prestipino, S. Kostlmeier, A. D. Corso and F. D. Di Tolla, *Science*, 2001, **291**, 288–290.
- 74 D. A. Tompsett, S. C. Parker and M. S. Islam, *J. Am. Chem. Soc.*, 2014, **136**, 1418–1426.
- 75 Y. Yuan, S. M. Wood, K. He, W. Yao, D. Tompsett, J. Lu, A. Nie, M. S. Islam and R. Shahbazian Yassar, *ACS Nano*, 2016, **10**, 539–548.
- 76 D. A. Tompsett and M. S. Islam, *J. Phys. Chem. C*, 2014, **118**, 25009–25015.
- 77 R. Hill, *Proc. Phys. Soc., London, Sect. A*, 1952, **65**, 349.
- 78 E. Riedo and H. Brune, *Appl. Phys. Lett.*, 2003, **83**, 1986–1988.
- 79 M. Shaari, N. Roselina, S. Kasolang, K. Hyie, M. Murad and M. Bakar, *J. Teknol.*, 2015, **76**(9), 69–73.
- 80 F. P. Bowden and D. Tabor, *Friction and Lubrication of solids, Part 1*, Oxford University Press, New York, 1950.
- 81 K. Johnson, *Contact Mechanics*, Cambridge University Press, Cambridge, 1987.
- 82 B. Persson, *Sliding friction: Physical principles and applications*, Springer, Berlin, 2nd edn, 2000.

